Research article

Digital twin with augmented state extended Kalman filters for forecasting electric power consumption of industrial production systems

A. Baldassarre [*], J.-L. Dion, N. Peyret, F. Renaud

Equipe Vibroacoustique, Structures et Formes Mécaniques - Laboratoire Quartz (EA 7393) - ISAE-Supméca, 3 rue Fernand Hainaut, Saint-Ouen CEDEX, 93407, France

ARTICLE INFO

ABSTRACT

The work aims to develop an effective tool based on Digital Twins (DTs) for forecasting electric power consumption of industrial production systems. DTs integrate dynamic models combined with Augmented State Extended Kalman Filters (ASEKFs) in a learning process. The connection with the real counterpart is realized exclusively through non-intrusive sensors. This architecture enables the model development of industrial systems (components, machinery and processes) on which complete knowledge is not available, by identifying the model's unknown parameters through short online training phases and small amounts of real-time raw data. ASEKFs track the unknowns keeping models updated as physical systems evolve. When a forecast is needed, the current estimates of the uncertain parameters are integrated into the dynamic models. These can then be used without ASEKFs to predict the actual energy use of the system under the desired operating conditions, including scenarios that differ from typical functioning. The approach is validated offline with reference to the electricity consumption of an automatic coffee machine, which represents a real test environment and a blueprint to design DTs for other industrial systems. The appliance is observed by measuring the supply voltage and the absorbed current. The accuracy of the results is analyzed and discussed. This method is developed in the context of energy consumption prediction and optimization in the manufacturing industry through refined energy management and planning.

1. Introduction

The industrial manufacturing sector accounts for a substantial part of the world economy and is among the sectors that consume most of the energy [1,2] and are responsible for most emissions [3]. It creates a vast variety of products on a wide range of scales, from small enterprises to big companies. Industries are constantly expanding and their energy consumption follows this growth [4]. Predicting and optimizing the industrial manufacturing energy usage and investigating its impact on the environment can make production more cost-efficient and sustainable.

Factories are approaching the Industry 4.0 model characterized by control automation, flexible production lines, modular production [5] and integration of smart sensors and Internet of Things [6]. Real-time data acquired throughout the plant enable a detailed

---

* Corresponding author.
  E-mail address: antonio.baldassarre@isae-supmeca.fr (A. Baldassarre).

energy consumption assessment for the single product production. This functionality can be extended to estimate future products' energy and monetary cost. Production processes can be dynamically adjusted, but administrators do not have a clear perspective of the consequences on energy consumption.

Energy consumption forecasting can be conducted with model-driven or data-driven techniques, addressing different levels of the industrial hierarchical structure: from individual machines to entire processes or sectors. Model-based approaches involve analytical and physical models, which require a large number of parameters that are often difficult to determine [7]. Data-driven methods are becoming popular due to progress in sensing technologies [8] and comprise statistical models, such as Non-Linear Regression and Multiple Linear Regression (MLR), and Machine Learning (ML) algorithms, such as Artificial Neural Network (ANN) and Support Vector Machine (SVM) [9].

In recent years, much effort has been put into evaluating and comparing the performance of data-driven approaches. MLR- and SVM-based models outperformed benchmark methods in short-term reactive power prediction in an Italian factory [10]. SVM and ANN provided more reliable results in terms of root mean square error (RMSE) than MLR and adaptive neuro-fuzzy inference system for long- and short-term electricity demand forecasting in Cyprus [11]. MLR performed best with a lower mean absolute percentage error (MAPE) than other ML algorithms for predicting energy consumption in industry in Morocco [12]. Deep Learning algorithms have been shown to improve the prediction performance of machine tool energy [13] and building cooling load [14] compared to popular techniques used in previous studies in the same fields. Data-driven techniques provide satisfactory results only with large amounts of historical data with minimum noise, as was proven in the case of ANN fed with a small, non-preprocessed dataset for forecasting appliance consumption in Smart Buildings [15].

This paper proposes a practical solution for forecasting electric power consumption of industrial systems based on Digital Twin (DT) technology. DTs are virtual replicas of units (components, machines), systems (processes, production systems, factories) or systems-of-systems (enterprise collaborations) and are spreading in various contexts, from healthcare to city management, thanks to developments in information technologies that enable the convergence between the cyber and physical worlds [16,17]. A DT is usually designed with a bi-directional data flow: it updates itself through real-time raw or preprocessed data as the physical counterpart to which it is bound evolves; by data processing, it provides useful insights that are then transferred to the real system to be exploited [17, 18]. In the industrial sector, DTs are applied throughout the entire product lifecycle [19] to accomplish different tasks: assembly line throughput optimization [20]; real-time monitoring and fault prediction/diagnosis in machine tools [21], aero-engines [22] and energy storage systems [23], enabling predictive maintenance [24]; energy consumption minimization, production scheduling and planning, and effective energy management with renewable energy integration [25].

The developed DT adopts a hybrid approach between model-driven and data-driven techniques, as it relies on gray-box models trained online by Augmented State Extended Kalman Filters (ASEKFs) through real-time data acquired from a few non-intrusive sensors. It aims to tackle the main drawbacks of these techniques, namely the need for detailed information on the real system to build a reliable physical model (model-driven methods) and large amounts of high-quality data to feed a statistical or ML algorithm (data-driven methods). Little knowledge about the system is used to deduce a virtual model whose parameters are identified by ASEKFs exploiting small raw datasets. Following the training phase, the DT provides online power consumption predictions and performance analysis under the desired system operating conditions. Its features ensure its implementation in industrial production sites without special efforts.

The paper is organized as follows: Section 2 presents the DT architecture with a brief introduction to the ASEKF and sets out the approach to modeling and observing the system; Section 3 describes the development of the system model; model training is discussed in Section 4, detailing the implementation of the ASEKFs and illustrating the findings of the identification process; power consumption prediction and model validation results are given in Section 5; conclusions are drawn in Section 6.

2. Digital twin architecture

The DT architecture comprises physical object, non-intrusive sensors, model, ASEKF algorithm, human-machine interface and data
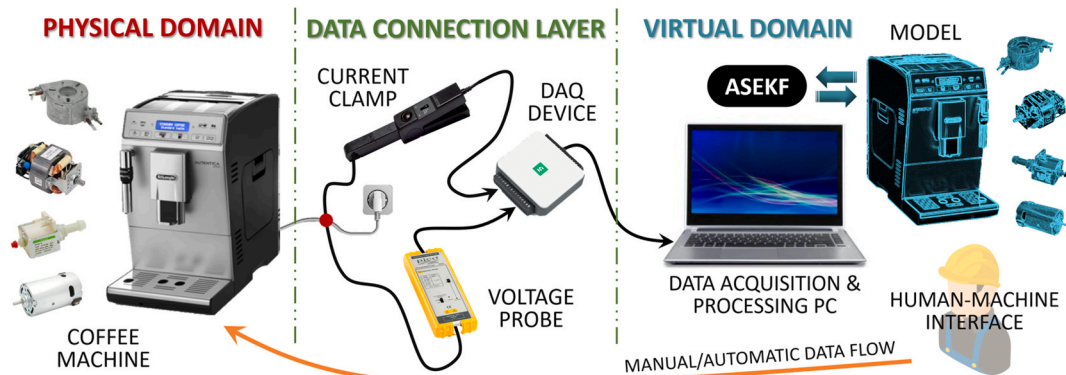

Fig. 1. DT architecture and data acquisition system.

integration systems. These technologies are organized into physical part, virtual part and data connection layer [26] (Fig. 1). This paper investigates the core of the architecture: the data flow from physical to virtual domain, the virtual model development and interconnection with the ASEKF, the data processing for model training and forecasting.

The sensors used to monitor the actual system are not intrusive, as they can be mounted outside it, but they may or may not be in contact with it. The technique requires the measurement of the supply voltage and the current drawn by the industrial electrical system. Specifically, it is possible to use a voltage probe and current clamp located on the power supply cable (see Section 2.4).

The DT can be synchronized in real time with the original counterpart through ASEKFs and is based on the analytical description of its physical behavior. The integration of the ASEKF algorithm into the DT architecture enables:

- virtual model development of systems about which only minimal knowledge is available, by identifying their unknown parameters through rapid unsupervised training phases and a few real-time raw data;
- online training, which follows the real system's evolution, tracking parameters and updating the virtual model to preserve the DT's accuracy.

When administrators or operators request the execution of a forecast, the current values identified for the unknown parameters are introduced into the virtual model. The model is then used without the ASEKF to simulate the behavior of the real system during the specified operating conditions, enabling the energy quantities of interest to be predicted. Forecast scenarios may be similar or deviate significantly from the standard operation of the system.

The human-machine interface allows the user to analyze forecast results and make decisions for production scheduling and planning. Depending on the way the knowledge generated in the virtual domain is then applied to the real one, the proposed structure can be deployed to design DTs (automatic data flow) or Digital Shadows (manual data flow) [27].

Since industrial systems are too constrained to easily verify and validate novel scientific methods, it is customary to test them on a laboratory system, which can be easily equipped and upgraded as required. The approach is described and validated with reference to an automatic coffee machine for domestic use, which automates the entire process from grinding coffee beans to brewing hot coffee. The experiment, and thus the validation, is conducted in offline mode, first acquiring data from the real system in operation and then processing it with the ASEKFs. This academic use-case provides a real-world context for testing strategies and methods, as it has analogies with industrial machines in terms of operating principle and type of components. The relevance of this laboratory system for industrial applications was demonstrated by evaluating its intrinsic scalability and similarity metrics with respect to several industrial use-cases [28]:

- an industrial device, i.e. a heating, ventilation and air-conditioning (HVAC) system for a vehicle test bench;
- a food manufacturing production line, i.e. a mixing, refining and conching line of a chocolate factory.

Using semantic similarity and in light of the prediction tool as the scientific approach to be validated, the coffee machine can symbolize an electric-powered industrial machine where there exists a basic understanding of the mechanisms behind the process being carried out. Some assumptions can be made about components and their characteristics without opening and disassembling the appliance, keeping the non-intrusiveness of the technique in place. From a broader perspective, the coffee machine can be representative of an industrial production line: the cup of coffee is the final product and the appliance's subsystems are the individual machines that perform a specific task along the process. The proposed method can therefore be scaled and applied to estimate the production line's power consumption.

2.1. Augmented state extended Kalman filter

The Kalman Filter algorithm [29] is a linear recursive state variable estimator. This algorithm and its numerous variants, such as the Extended Kalman Filter (EKF) and the Unscented Kalman Filter, are widely applied in navigation, guidance and robotics technologies (position estimation, trajectory tracking and object detection), and are also suitable for solving problems in many other fields, such as econometrics and medicine [30]. In industrial electronics, the main implementations concern signal processing and instrumentation, electric motor sensorless control and health monitoring, and other control systems [31], as well as energy storage systems for charge state estimation [32–34]. The Augmented State Kalman Filter effectively deals with models containing parameters which deviate from nominal values due to unknown biases, by including the bias terms in the state vector [35]. This feature is exploited in many studies, such as force identification in structural dynamics [36] and modulated sinusoidal component tracking in signal processing [37].

The proposed ASEKF technique consists of an EKF [38] applied to an augmented state-space model, in which the model's unknown parameters are added to the state vector.

The EKF is a data assimilation algorithm for state variable estimation of non-linear systems and can be split into two steps:

- prediction; the state estimate and its uncertainty are predicted through the system dynamic model;
- correction; the state estimate is updated by exploiting the observations obtained through sensors.

The algorithm can be used in real time and successfully handles uncertainties due to noisy data and model approximations. Although the dynamics of the physical system is continuous time, the EKF usually needs to be implemented in digital computers.

Therefore, the dynamics is discretized and the discrete-time model of the non-linear system can be expressed as:

$$\mathbf{z}_k = f\left(\mathbf{z}_{k-1}, \mathbf{q}_{k-1}, \mathbf{u}_{k-1}\right) + \mathbf{w}_{k-1} \tag{1}$$

$$\mathbf{y}_k = g\left(\mathbf{z}_k, \mathbf{q}_k\right) + \mathbf{v}_k \tag{2}$$

where

- k is the time index;
- $\mathbf{z}_k$ is the state vector at time k;
- $\mathbf{q}_{k-1}$ is the vector of unknown model parameters at time $k-1$;
- $\mathbf{u}_{k-1}$ is the control input vector at time $k-1$;
- $\mathbf{w}_{k-1}$ is the process noise vector at time $k-1$;
- $\mathbf{y}_k$ is the measurement vector (observation) at time k;
- $\mathbf{v}_k$ is the measurement noise vector at time k;
- f is the state transition function;
- g is the observation function.

Equations (1) and (2) are called discrete-time state equation and discrete-time observation equation, respectively. Process noise $\mathbf{w}$ and measurement noise $\mathbf{y}$ are assumed to be additive terms and multivariate normal distributions with zero mean and covariance matrices $\mathbf{Q}$ and $\mathbf{R}$, respectively. The covariance matrix $\mathbf{Q}$ takes into account uncertainties due to modeling approximations, while the covariance matrix $\mathbf{R}$ accounts for the uncertainty due to measurement noise.

To derive the augmented state-space model, the discrete-time state equation (1) is supplemented with an equation relating the unknown parameter vector $\mathbf{q}$ at time $k-1$ and time k. Due to the lack of prior information on the time evolution of uncertain parameters, a discrete-time random-walk model is adopted to describe their dynamics [36,39]:

$$\mathbf{q}_k = \mathbf{q}_{k-1} + \mathbf{w}_{k-1}^q \tag{3}$$

where the noise vector $\mathbf{w}_k^q$, which accounts for the parameter increment, is assumed to be a zero-mean multivariate normal distribution with associated covariance matrix $\mathbf{Q}^q$. Equation (3) allows the time trend of unknown parameters to be estimated through an appropriate calibration of the covariance $\mathbf{Q}^q$. The augmented state vector $\mathbf{z}_k^a$ is defined as:

$$\mathbf{z}_k^a = \begin{bmatrix} \mathbf{z}_k \\ \mathbf{q}_k \end{bmatrix} \tag{4}$$

The augmented state equation is obtained by combining equations (1) and (3), and introducing the definition (4):

$$\mathbf{z}_k^a = f^a\left(\mathbf{z}_{k-1}^a, \mathbf{u}_{k-1}\right) + \mathbf{w}_{k-1}^a \tag{5}$$

where f^a is the augmented state transition function and $\mathbf{w}_k^a$ is the augmented process noise vector

$$\mathbf{w}_k^a = \begin{bmatrix} \mathbf{w}_k \\ \mathbf{w}_k^q \end{bmatrix} \tag{6}$$

with associated augmented covariance matrix $\mathbf{Q}^a$, expressed as:

$$\mathbf{Q}^a = \begin{bmatrix} \mathbf{Q} & \mathbf{0} \\ \mathbf{0} & \mathbf{Q}^q \end{bmatrix} \tag{7}$$

In the augmented state-space model, the discrete-time observation equation (2) becomes

$$\mathbf{y}_k = g^a\left(\mathbf{z}_k^a\right) + \mathbf{v}_k \tag{8}$$

where g^a is the augmented observation function.

The discrete-time ASEKF is formulated as follows:

Prediction step

$$\widehat{\mathbf{z}}_{k|k-1}^a = f^a\left(\widehat{\mathbf{z}}_{k-1|k-1}^a, \mathbf{u}_{k-1}\right) \tag{9}$$

$$\mathbf{F}_k = \left.\frac{\partial f^a}{\partial \mathbf{z}_{k-1}^a}\right|_{\widehat{\mathbf{z}}_{k-1|k-1}^a, \mathbf{u}_{k-1}} \tag{10}$$

$$\mathbf{P}_{k|k-1} = \mathbf{F}_k \mathbf{P}_{k-1|k-1} \mathbf{F}_k^T + \mathbf{Q}^a \tag{11}$$

Correction step

$$\mathbf{G}_k = \left.\frac{\partial \mathbf{g}^a}{\partial \mathbf{z}_k^a}\right|_{\widehat{\mathbf{z}}_{k|k-1}^a} \tag{12}$$

$$\mathbf{K}_k = \mathbf{P}_{k|k-1}\mathbf{G}_k^T \left(\mathbf{G}_k \mathbf{P}_{k|k-1}\mathbf{G}_k^T + \mathbf{R}\right)^{-1} \tag{13}$$

$$\widehat{\mathbf{y}}_k = \mathbf{g}^a\left(\widehat{\mathbf{z}}_{k|k-1}^a\right) \tag{14}$$

$$\widehat{\mathbf{z}}_{k|k}^a = \widehat{\mathbf{z}}_{k|k-1}^a + \mathbf{K}_k(\mathbf{y}_k - \widehat{\mathbf{y}}_k) \tag{15}$$

$$\mathbf{P}_{k|k} = (\mathbf{I} - \mathbf{K}_k\mathbf{G}_k)\mathbf{P}_{k|k-1} \tag{16}$$

The variables that appear in equations 9–16 are defined in Table 1.

The ASEKF can diverge due to inappropriate initialization, severe non-linearities or insufficient information given by the measurements. It is essential to test its performance with synthetic data, checking whether it converges and correctly identifies parameters. Once convergence tests are successful, the algorithm is fed with real data.

2.2. Modeling approach

Mathematical modeling of industrial systems is addressed with white-box, black-box or gray-box models. In general, prior knowledge and experimental data are the sources of information for model development. White-box modeling uses the first source and implies that all the required knowledge is available. The model is built by using scientific governing equations and supplementary equations that describe the system's behavior. Black-box modeling is applied when there is no information accessible. It exploits experimental measurements of system inputs and outputs to develop parametric models whose parameters have no physical meaning. Since repeating the experiment might lead to different models, result reproducibility is not assured. Gray-box modeling relies on both sources to overcome the shortcomings of previous approaches [40].

At many industrial sites, knowledge of the production line machinery and equipment is only partial. Although the operation carried out by a given machine may be well known, the available information on the components and their technical specifications is not sufficient to build a white-box model. If adequate experiments can be conducted, the gray-box approach is the most suitable. According to the way prior knowledge is exploited, gray-box modeling is classified into constrained black-box identification, semi-physical, mechanistic, hybrid and distributed parameter modeling. Following the mechanistic modeling, a preliminary model with scientific equations is formulated on the basis of prior information and its unknown elements are estimated through experimental data. This model can then be fine-tuned by examining the residuals [41].

Since the DT's objective is the electricity consumption prediction, the machine is modeled from an electrical point of view by investigating the most energy-consuming components. Only subsystems contributing more than 1% of the appliance's power rating (1450 W [42]) are considered. Four main subsystems can be distinguished: the coffee grinder, the electric pump, the boiler and the infuser. Each of these is associated with an elementary working phase: coffee grinding, water pumping, water heating and infuser positioning. Components characterized by a power rating of less than 14.5 W, but operating for a much longer time than those typical of the four phases identified, can become significant in terms of energy consumption. However, detecting the nature of these electrical devices can be difficult and their electrodynamic behavior cannot be adequately investigated: the acquisition system used to observe the appliance does not allow to obtain reliable measurements for such weak current signals, with a rms value lower than 60 mA (see Section 2.4).

The modeling technique adopted is the lumped parameter approach, which assumes that the attributes of the spatially distributed physical system are concentrated in discrete elements [43,44]. Knowledge of the process is exploited to build equivalent electrical circuits made up of lumped elements, such as resistors, inductors and capacitors. By applying Kirchhoff's voltage law, circuits provide dynamic models consisting of continuous ordinary differential equations, which contain parameters having a specific physical

Table 1
Variables of the ASEKF.

Variable	Definition
$\widehat{\mathbf{z}}_{k|k-1}^a$	*a priori* augmented state estimate at time k
$\widehat{\mathbf{z}}_{k|k}^a$	*a posteriori* augmented state estimate at time k
$\mathbf{P}_{k|k-1}$	*a priori* estimate covariance matrix at time k
$\mathbf{P}_{k|k}$	*a posteriori* estimate covariance matrix at time k
$\mathbf{F}_k$	Jacobian of f^a at time k
$\mathbf{G}_k$	Jacobian of g^a at time k
$\mathbf{K}_k$	Kalman gain at time k
$\widehat{\mathbf{y}}_k$	observation estimate at time k
$\mathbf{I}$	identity matrix

meaning. The electrical systems analyzed are characterized by non-linearity. In the model development, parasitic capacitances and iron losses (hysteresis and eddy currents losses) in magnetic circuit are neglected; the magnetization characteristic of ferromagnetic materials is considered linear (magnetic saturation is ignored) [43].

Equation parameters are the model's unknown elements and can be time-invariant or time-variant. Their time history is estimated by combing the dynamic models with ASEKFs: the uncertain parameters are included in the augmented state vector of the algorithm, which will provide insights into them. To enable the implementation of ASEKFs, the continuous dynamic models obtained must be discretized in the time domain.

In addition to dynamic models useful for describing the electrical behavior of the systems under investigation, others are developed to study their mechanical behavior. Mechanical models are not included in the DT architecture. They are intended to obtain a better understanding of the systems' global dynamics by investigating the phenomena that give rise to non-linearities.

2.3. Model validation criterion

The equivalent electrical circuits developed from prior information are preliminary models and must be validated: a circuit is accepted if it can accurately estimate the power consumption of the actual subsystem. If the ASEKF converges, the identified parameters are introduced into the dynamic model, which is then employed without the filter to predict the electrical circuit instantaneous power.

The prediction accuracy is evaluated using the root mean square error (RMSE) and the coefficient of variation of the RMSE (CV-RMSE):

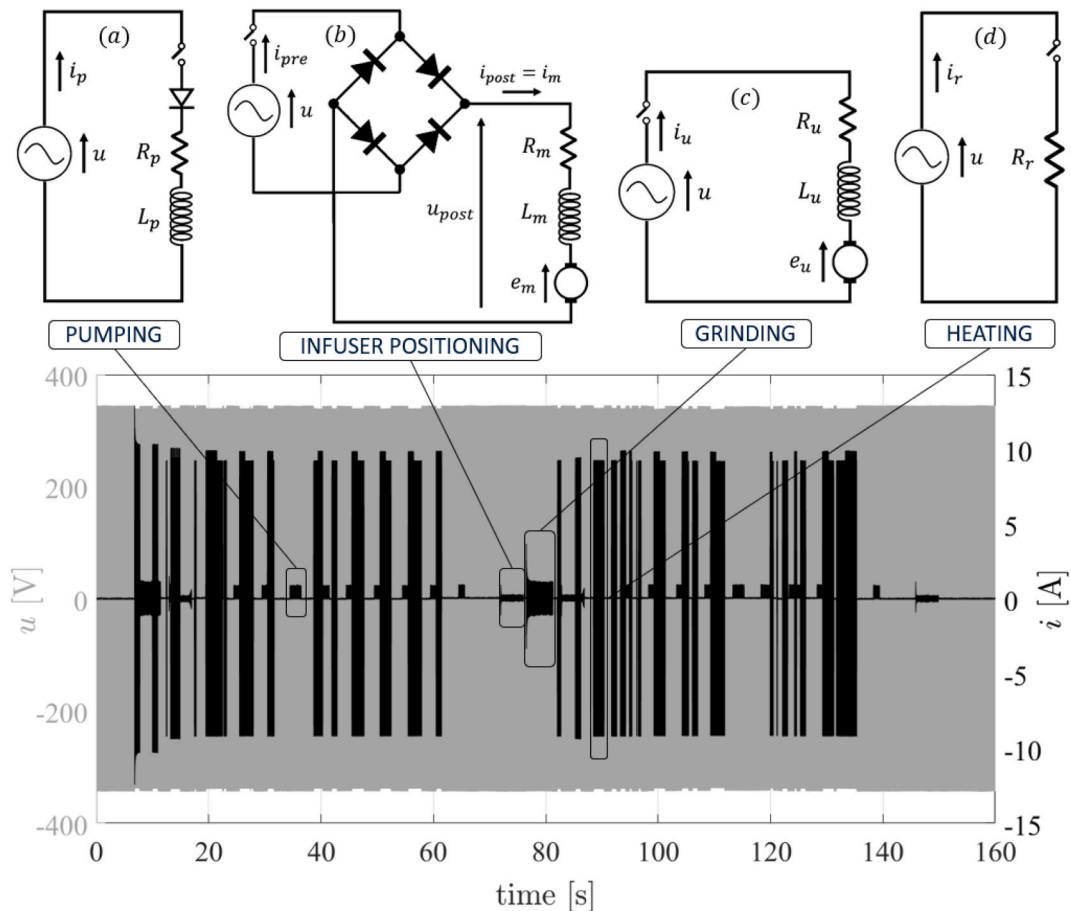$$\mathrm{RMSE} = \sqrt{\frac{1}{n} \sum_{k=1}^{n} (p_k - \widehat{p}_k)^2} \qquad (17)$$

Fig. 2. Voltage u and current i measurements (*coffee1*). Phase circuit diagrams.

$$\mathrm{CV} - \mathrm{RMSE} = \frac{\sqrt{\frac{1}{n}\sum\limits_{k=1}^{n}\left(p_k - \widehat{p}_k\right)^2}}{\frac{1}{n}\sum\limits_{k=1}^{n}p_k} \tag{18}$$

where p_k and $\widehat{p}_k$ are the actual and predicted values at time k, respectively, and n is the number of samples. The mean absolute percentage error (MAPE) is not applicable since the denominator can be close zero. Several situations may arise:

- CV-RMSE < 15%; the predicted instantaneous power $\widehat{p}$ accurately approximates the measured power p; the model can be validated;
- 15% ≤ CV-RMSE < 25%; the forecast $\widehat{p}$ fairly approximates the measured curve p, but not satisfactorily; if the training process has room for improvement, the parameter identification can be fine-tuned; otherwise, the electrical circuit can be slightly modified making new assumptions;
- the predicted power $\widehat{p}$ is unable to track the actual power p; the pre-liminary model is not suitable and must be replaced.

If the ASEKF does not converge, the training fails and the model is discarded without validation, no matter whether it faithfully represents the subsystem dynamics or not. As its unknown parameters cannot be identified, the model is useless for predicting power consumption. The equivalent circuits that successfully passed the validation test are depicted in Fig. 2.

2.4. System observation

At industrial sites, sensors enable data collection from machines and the environment, ensuring monitoring and a deeper comprehension of the manufacturing process. Standard sensors only collect data, whereas smart sensors also integrate the functionality of processing raw data locally, triggering specific operations or transmitting data to computer systems [6].

The introduction of a sensor network in a factory not only entails new costs, but may require the production shutdown during installation and profound changes to the machinery structure. The connection between the DT and its real counterpart is realized through non-intrusive sensors, which are placed externally to the system and do not interfere with its operation. In this way, the sensor grid installation is effortless, as it does not involve excessive modifications to the machines.

The coffee machine is powered by the French electricity mains. The observed variables are the single-phase AC supply voltage u and the total current i absorbed by the appliance. The former is measured through a differential probe, whereas the latter by a current clamp based on Hall effect. The sensors are placed on the power supply cable of the machine (Fig. 1). In particular, the clamp can be positioned and removed without interrupting the process. Data are acquired using the NI USB-6003 DAQ device at a sampling frequency of 6250 Hz (time resolution $\Delta t = 1.6 \times 10^{-4}$ s). Table 2 lists sensor technical specifications. Sensor accuracy is expressed as a percentage of the reading plus an offset, defined as the value that exists when the measurement should be zero.

Three different datasets are analyzed: *coffee1.mat*, *coffee2.mat* and *coffee3.mat* from the *CAFFEINE Dataset* [45] (CAFFEINE_Dataset/dataset/coffee_matlab_sample). Data acquisitions refer to the long coffee mode, which dispenses the largest amount of product (about 200 ml) and is chosen as representative of the appliance's behavior. By switching mode, the coffee quantity and brew strength can be altered, but the process remains qualitatively the same; only the duration of some elementary phases changes.

The first acquisition is shown in Fig. 2, where the four elementary phases are associated with the equivalent circuits of the corresponding subsystems. During an elementary working phase, only one subsystem is in operation. The phase sequence (switching on/off of each subsystem) is deduced through prior knowledge of the process [46] and preliminary analysis of the current measurement i (Fig. 2) in combination with the observation of the appliance's behavior.

The water heating phase is easy to detect, as it absorbs the most energy, due to the water high heat capacity. The current reaches a peak close to 10 A during heating. At the beginning of the process, the machine grinds coffee beans. The ground coffee is collected by the infuser of the brew group, which is moved to the brewing position tamping the powder into a compact puck. An electric pump draws fresh water from the tank and delivers it to the boiler. The hot water is then forced through the infuser to extract the soluble substances from the coffee and produce the so-called espresso. Multiple pumping phases take place and, at the end of the brewing process, the infuser is returned to its original location, ready to receive new ground coffee. Therefore, the grinding phase (performed twice in long coffee mode) is followed by two infuser positionings, where the brew unit moves back and forth along the same path. Automatic coffee machines have also built-in sensors. Temperature probes regulate the boiler functioning, according to the attainment of the brew water set point temperature (about 90 °C). Whenever the set point is reached, water pumping is enabled. When the required water quantity has passed through the in-line flow meter, the pump is turned off. Water heating is the only phase that can occur simultaneously with another.

Table 2
Sensor technical specifications.

Sensor	Current	Voltage
Sensitivity	100 mV/A	1/200
Range	from −10 A to 10 A	from −1400 V to 1400 V
Accuracy	±(3%+50 mA)	±(2%+1 V)
Noise level (output)	3 mV (peak-to-peak)	0.7 mV (rms)

Fig. 3 shows a 3-cycle zoom of the measurements for each elementary phase when the corresponding subsystem is operating at steady state. The variables i_p, i_{pre}, i_u and i_r denote the current drawn by the appliance during water pumping (graph (a)), infuser positioning (graph (b)), coffee grinding (graph (c)), and water heating (graph (d)), respectively. The investigated subsystems are characterized by different dynamics. Preliminary analysis of the current waveform helps to understand whether these are characterized by linear or non-linear behaviors and to justify some of the choices made in the modeling. Such analysis can complement prior knowledge of the process and support in the construction of the equivalent electrical circuit, in a sort of reverse engineering (see Sections 3.1 and 3.2). Subsystems' transient behavior is not studied.

The four circuits (Fig. 2) are connected in parallel. Since the voltage probe is placed on the power cable, the measurement u coincides with the actual voltage across the load and the power socket internal resistance is omitted during model development. The French electricity distribution network delivers an alternating voltage that ideally has a sinusoidal waveform of constant frequency (50 Hz) and amplitude (230 V rms). However, the actual wave is never perfectly sinusoidal and its frequency and amplitude vary constantly due to disturbances in the electricity grid. The regulations require the supplier to ensure a rms value between 90% and 110% of the nominal value [47]. The rms of u is approximately 242.8 V. The FFT of the signal reveals that its frequency is about 49.95 Hz and its harmonic content is not limited to the fundamental frequency, but there is also energy in the higher harmonics, especially the odd ones.

Model training and power consumption prediction are performed separately for each subsystem, by referring to the relevant phase and assuming that the total current absorbed by the machine coincides with the current drawn by the subsystem. An ASEKF is therefore implemented for each sub-system.

3. System modeling

3.1. Water pumping subsystem

Since coffee percolation requires high pumping pressure (about 10 bar) and accurate flow regulation, the most commonly used electric device in home coffee machines is the solenoid pump. The cost and the encumbrance of centrifugal pumps are justified only for professional usage [46,48]. Solenoid pumps are reciprocating-type positive displacement pumps and compress a fixed amount of liquid within a pressure chamber through a spring-loaded piston moved by an electromechanical solenoid [49,50].

A solenoid comprises a fixed housing, a copper coil and a moving ferro-magnetic armature (the piston) [51–53]. A schematic representation of the pump solenoid is depicted in Fig. 4: $x(t)$ is the armature position, k_1 and k_2 are the compression springs stiffnesses,
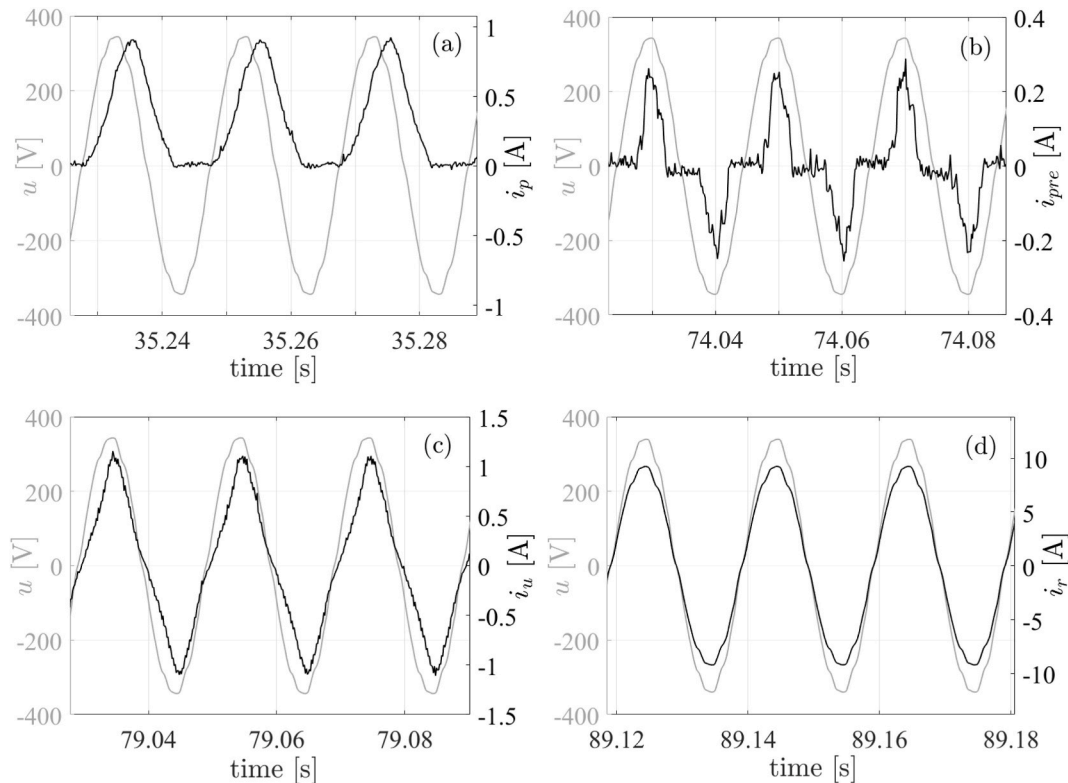

Fig. 3. Voltage u and current measurements, 3-cycle zoom (*coffee1*): water pumping (a), infuser positioning (b), coffee grinding (c), water heating (d).
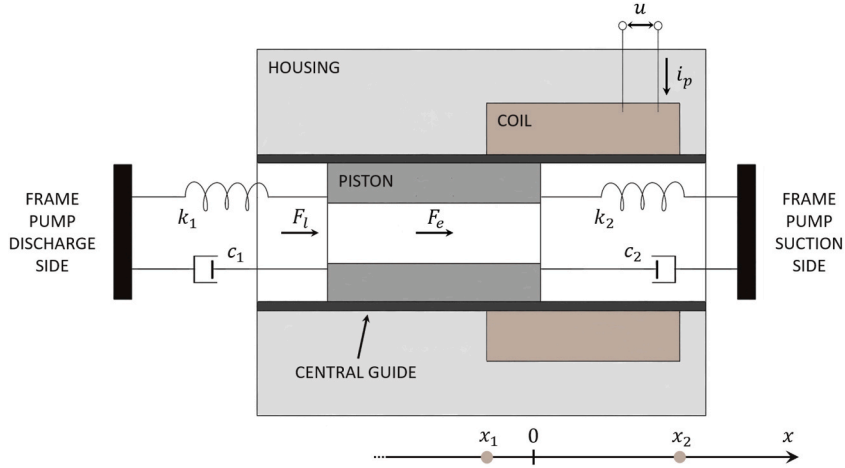
Fig. 4. Pump solenoid diagram.

c_1 and c_2 are the viscous damping coefficients representing the friction between the non-magnetic central guide and the piston coating, $F_l(t)$ is the load exerted on the piston by the fluid pressure during the pumping stroke, $F_e(t)$ is the solenoid electromagnetic force. The solenoid inductance $L_p(x)$ varies monotonically between the coil ends x_1 and x_2 [54]. The piston dynamics can be described using the following equation [51,52,55]:

$$m\frac{d^2x(t)}{dt^2} + (c_1 + c_2)\frac{dx(t)}{dt} + (k_1 + k_2)x(t) = F_e(t) + F_l(t) \tag{19}$$

where m is the piston mass.

In the absence of power, the piston is in equilibrium position $x = 0$. When power is applied, during the positive half of the voltage cycle (suction stroke, $\frac{dx(t)}{dt} > 0$), current flows through the wire and the resulting magnetic field attracts the piston inside the coil, increasing $L_p(x)$. The electromagnetic force is produced by the change in inductance with the position $x(t)$ and can be expressed as [51, 54]:

$$F_e(t) = \frac{1}{2}i_p^2(t)\frac{dL_p(x)}{dx} \tag{20}$$

where $i_p(t)$ is the current flowing in the pump.

An integrated diode inside the coil allows the current to flow in only one direction. During the negative half of the voltage cycle (pumping stroke, $\frac{dx(t)}{dt} < 0$), $F_e(t)$ vanishes because $i_p(t)$ drops to zero, and the return spring pushes the piston towards the front of the pump.

The variable inductance $L_p(x)$ and the diode introduce non-linearities in the electrical system. Graph (a) in Fig. 3 shows the current $i_p(t)$ drawn by the electric pump. The pump operating speed is determined by the voltage frequency to which it is connected. A pumping cycle occurs in about 0.02 s and is divided into two portions: the first, where $i_p(t)$ is positive and $F_e(t)$ is produced; the second, where $i_p(t)$ is null because of the diode.

The pump's electrodynamic behavior is described by using the electrical circuit (a) in Fig. 2 [55]: R_p is the coil resistance; the diode is ideal. The state equation of the pumping phase is derived by applying Kirchhoff's voltage law to the circuit [51,55]:

$$u(t) = \left(R_p + \frac{dL_p(x)}{dx}\frac{dx(t)}{dt}\right)i_p(t) + L_p(x)\frac{di_p(t)}{dt} \tag{21}$$

Electrical model (21) and mechanical model (19) are coupled through the piston velocity $\frac{dx(t)}{dt}$, the current $i_p(t)$ and the inductance $L_p(x)$.

To simplify the model (21), it is reasonable to assume that the amplitude of variation of the term $\frac{dL_p(x)}{dx}\frac{dx(t)}{dt}$ is much smaller than the electrical resistance R_p and to verify a posteriori, after the training and prediction procedures, whether the model is able to provide adequate results. Consequently, $\frac{dL_p(x)}{dx}\frac{dx(t)}{dt}$ is neglected and equation (21) becomes:

$$u(t) = R_p i_p(t) + L_p(x)\frac{di_p(t)}{dt} \tag{22}$$

This equation only applies to the description of the circuit dynamics during the first part of each pumping cycle ($i_p(t) > 0$). In the second part, $i_p(t)$ is simply set to zero and kept constant as long as $u(t)$ remains negative. When $u(t)$ becomes positive, equation (22)

applies again. The integration conditions that determine the transition from the first to the second part of the cycle are

$$i_p(t) = 0 \tag{23}$$

$$u(t) < 0 \tag{24}$$

The condition that defines the transition to the next cycle is

$$u(t) \geq 0 \tag{25}$$

The unknown parameters of equation (22) are the time-varying inductance $L_p(t)$ and the constant resistance R_p. The discrete-time state equation for the pumping phase is obtained by discretizing equation (22) using the explicit (forward) Euler's method [56]:

$$i_{p,k} = i_{p,k-1} + \frac{\Delta t}{L_{p,k-1}} \left(u_{k-1} - R_{p,k-1} i_{p,k-1} \right) \tag{26}$$

where Δt is the time step.

3.2. Coffee grinding subsystem

The process is performed by a grinder. Coffee beans are fed through a gap of progressively decreasing width between a pair of cutting tools: one fixed and one movable which is driven by an electric motor [57]. Since beans need to be reduced to powder quickly to speed up the process, the most commonly used electric device is the universal motor [58], which can reach speeds of several thousand rpm and is suitable for domestic appliances thanks to its light weight and compactness [59–62]. If more accurate particle size control is required, DC motors with low speed and high torque are usually adopted. They improve the powder fineness and uniformity, but slow down the whole process [58].

Graph (c) in Fig. 3 shows the current $i_u(t)$ absorbed by the electric motor. The cycle period is about 0.02 s and is determined by the mains voltage frequency. The signal $i_u(t)$ can be traced back to that of an electric motor operating directly on AC power. A DC motor would require a rectifier, resulting in a significantly different current signal. The grinding phase is fast (about 5 s) and a noisy motor is observed during tests. These aspects suggest the presence of a universal motor, which is therefore assumed to be installed in the machine. The current $i_u(t)$ exhibits a pseudo-triangular waveform. The input voltage $u(t)$ is also not a perfect sine wave, but the two signals do not have the same shape: $i_u(t)$ is more distorted because the presence of odd harmonics in its frequency spectrum is more pronounced. This means that the system is non-linear. In electric motors, non-linearity can arise from various phenomena, for example from magnetic core saturation [43,60,63,64]. However, in the model development, saturation and armature reaction are considered negligible and non-linearities are assumed to originate from the coupled mechanical system.

The universal motor's electrodynamic behavior is described through the electrical circuit (c) in Fig. 2 [60]: R_u includes the resistances of brushes, field and armature windings; L_u comprises the field and armature windings inductances; $e_u(t)$ is the universal motor back-electromotive force. The state equation of grinding phase is obtained by applying Kirchhoff's voltage law to the circuit [60, 65,66]:

$$u(t) = R_u i_u(t) + L_u \frac{di_u(t)}{dt} + e_u(t) \tag{27}$$

where $e_u(t)$ can be approximated with the expression of the back-electromotive force of a DC series motor:

$$e_u(t) = K_a K_f i_u(t) \omega_u(t) \tag{28}$$

with K_a being the armature constant, K_f the field constant and $\omega_u(t)$ the motor speed. By introducing expression (28), equation (27) becomes:

$$u(t) = \widetilde{R}_u(t) i_u(t) + L_u \frac{di_u(t)}{dt} \tag{29}$$

where

$$\widetilde{R}_u(t) = R_u + K_a K_f \omega_u(t) \tag{30}$$

The resistance $\widetilde{R}_u(t)$ varies as a function of the speed $\omega_u(t)$.

The unknown parameters of equation (29) are the constant inductance L_u and the time-varying resistance $\widetilde{R}_u(t)$. The discrete-time state equation for the grinding phase is derived by discretizing equation (29) through the explicit Euler's method:

$$i_{u,k} = i_{u,k-1} + \frac{\Delta t}{L_{u,k-1}} \left(u_{k-1} - \widetilde{R}_{u,k-1} i_{u,k-1} \right) \tag{31}$$

where Δt is the time step.

The speed $\omega_u(t)$ is determined by the load connected to the motor: when the load increases, the speed $\omega_u(t)$ and the back-

electromotive force $e_u(t)$ decrease, resulting in an increase in the current $i_u(t)$. If a speed limit is not introduced, universal motors running with no load or light load can reach such a high speed that they can be damaged. Consequently, they are typically connected to the load directly or through gears [60–62]. In the coffee machine, capacitive sensors detect the bean basket filling level: if there are not enough beans, the grinding is not started, avoiding the no-load condition.

The mechanical behavior of the universal motor can be described by the following equation [43,60,65,66]:

$$J\frac{d\omega_u(t)}{dt} + C\omega_u(t) = T_e(t) - T_l(t) \tag{32}$$

where J is the rotor moment of inertia, C is the viscous damping coefficient representing friction in bearings and air resistance experienced by rotating parts, $T_l(t)$ is the load torque and $T_e(t)$ is the motor electromagnetic torque, whose expression is:

$$T_e(t) = K_a K_f i_u^2(t) \tag{33}$$

If a gear transmission is used, equation (32) is still applicable, but J and C are equivalent parameters of the transmission and $T_l(t)$ is corrected by the transmission ratio. Electrical model (29) and mechanical model (32) are coupled through the motor speed $\omega_u(t)$ and the current $i_u(t)$.

The load $T_l(t)$ is represented by the resistance offered by the roasted coffee beans to grinding. The main factors influencing the bean strength are roasting, which gives it a brittle behavior, and water quenching, which can result in residual water, enhancing its tenacity. A batch of beans is a blend of coffee of several varieties and origins processed using different techniques, and thus has uneven hardness distribution [57,67]. A quantitative study of the energy required to fracture individual particles is possible for solids with simple geometry and stress states [68,69], but a coffee bean does not have a regular shape and homogeneous, isotropic material [57]. An estimation of $T_l(t)$ also necessitates the investigation of the comminution kinetics through stochastic theories [69]. However, this is beyond the scope of this paper. The qualitative analysis provides evidence of the chaotic nature of the load, which could be one of the phenomena causing the non-linearity of the system. Indeed, the particles have different geometry, size and mechanical strength, and the number of particles in contact with the cutters varies over time.

3.3. Infuser positioning and water heating subsystems

Graph (b) in Fig. 3 depicts the current $i_{pre}(t)$ drawn by the infuser positioning subsystem, whose behavior is described by the circuit (b) in Fig. 2, consisting of a full-wave rectifier with four ideal diodes [62,70,71] and the typical DC motor model [43,65]. The rectifier introduces non-linearities in the system. For the sake of brevity, results concerning this subsystem, which is the least energy-consuming (power rating below 18 W), are not presented.

In household appliances, the boiler is usually an electric heater converting electrical energy into heat (Joule effect). Its structure consists of a metal block which encloses the hydraulic circuit and the heating resistor [46,72]. Graph (d) in Fig. 3 shows the current $i_r(t)$ adsorbed by the electric heater, whose behavior is described using the circuit (d) in Fig. 2. The relationship between $u(t)$ and $i_r(t)$ can be expressed by a linear algebraic equation (Ohm's law). In this case, the ASEKF is not implemented, since the constant electrical resistance R_r of the heater can be identified through the least-squares solution [56].

4. Model training

4.1. Implementation of the ASEKFs

The state equation, unknown parameter vector, augmented state vector, input and observation of the ASEKF are given in Table 3 for each subsystem. The measured voltage u is considered as a known input.

The augmented state equation of the ASEKF for the pumping subsystem is obtained by combining the discrete-time state equation (26) and the discrete-time random-walk model (3) applied to the vector $\mathbf{q}_p$:

$$\widehat{\mathbf{z}}^a_{p,k|k-1} = \mathbf{f}^a_p\left(\widehat{\mathbf{z}}^a_{p,k-1|k-1}, u_{k-1}\right)$$

Table 3
Implementation of the ASEKFs.

Subsystem	Pumping	Grinding
State equation	eq. (26)	eq. (31)
$\mathbf{q}$	$\mathbf{q}_p = \{\, L_p \quad R_p \,\}^T$	$\mathbf{q}_g = \{\, L_u \quad \widetilde{R}_u \,\}^T$
$\mathbf{z}^a$	$\mathbf{z}^a_p = \{\, i_p \quad L_p \quad R_p \,\}^T$	$\mathbf{z}^a_g = \{\, i_u \quad L_u \quad \widetilde{R}_u \,\}^T$
Input	u	u
Observation	i_p	i_u

$$\left\{ \begin{array}{c} \widehat{i}_{p,k|k-1} \\ \widehat{L}_{p,k|k-1} \\ \widehat{R}_{p,k|k-1} \end{array} \right\} = \left\{ \begin{array}{c} \widehat{i}_{p,k-1|k-1} + \dfrac{\Delta t}{\widehat{L}_{p,k-1|k-1}}\left(u_{k-1} - \widehat{R}_{p,k-1|k-1}\,\widehat{i}_{p,k-1|k-1}\right) \\ \\ \widehat{L}_{p,k-1|k-1} \\ \\ \widehat{R}_{p,k-1|k-1} \end{array} \right\} \tag{34}$$

There is no dynamic equation expressing the unknown parameters' evolution; their trends are tracked thanks to the probabilistic component of the algorithm. The Jacobian of f_p^a is

$$\mathbf{F}_{p,k} = \left.\begin{bmatrix} 1 - \Delta t \dfrac{R_{p,k-1}}{L_{p,k-1}} & \dfrac{\Delta t}{L_{p,k-1}^2}\left(R_{p,k-1}i_{p,k-1} - u_{k-1}\right) & -\Delta t \dfrac{i_{p,k-1}}{L_{p,k-1}} \\ 0 & 1 & 0 \\ 0 & 0 & 1 \end{bmatrix}\right|_{\widehat{\mathbf{z}}_{p,k-1|k-1}^a} \tag{35}$$

The augmented observation equation of the ASEKF for the pumping subsystem is

$$\widehat{i}_{p,k} = g_p^a\left(\widehat{\mathbf{z}}_{p,k|k-1}^a\right) = \widehat{i}_{p,k|k-1} \tag{36}$$

The Jacobian of g_p^a is constant:

$$\mathbf{G}_p = \begin{bmatrix} 1 & 0 & 0 \end{bmatrix} \tag{37}$$

Similarly, the ASEKF is implemented for the grinding subsystem. The augmented state equation is obtained by combining equation (31) and the random-walk progression (3) applied to the vector $\mathbf{q}_g$:

$$\widehat{\mathbf{z}}_{g,k|k-1}^a = \mathbf{f}_g^a\left(\widehat{\mathbf{z}}_{g,k-1|k-1}^a, u_{k-1}\right)$$

$$\left\{ \begin{array}{c} \widehat{i}_{u,k|k-1} \\ \widehat{L}_{u,k|k-1} \\ \widehat{\widehat{R}}_{u,k|k-1} \end{array} \right\} = \left\{ \begin{array}{c} \widehat{i}_{u,k-1|k-1} + \dfrac{\Delta t}{\widehat{L}_{u,k-1|k-1}}\left(u_{k-1} - \widehat{\widehat{R}}_{u,k-1|k-1}\,\widehat{i}_{u,k-1|k-1}\right) \\ \\ \widehat{L}_{u,k-1|k-1} \\ \\ \widehat{\widehat{R}}_{u,k-1|k-1} \end{array} \right\} \tag{38}$$

The Jacobian of f_g^a is

$$\mathbf{F}_{g,k} = \left.\begin{bmatrix} 1 - \Delta t \dfrac{\widetilde{R}_{u,k-1}}{L_{u,k-1}} & \dfrac{\Delta t}{L_{u,k-1}^2}\left(\widetilde{R}_{u,k-1}i_{u,k-1} - u_{k-1}\right) & -\Delta t \dfrac{i_{u,k-1}}{L_{u,k-1}} \\ 0 & 1 & 0 \\ 0 & 0 & 1 \end{bmatrix}\right|_{\widehat{\mathbf{z}}_{g,k-1|k-1}^a} \tag{39}$$

The augmented observation equation of the ASEKF for the grinding subsystem is

$$\widehat{i}_{u,k} = g_g^a\left(\widehat{\mathbf{z}}_{g,k|k-1}^a\right) = \widehat{i}_{u,k|k-1} \tag{40}$$

The Jacobian of g_g^a is

$$\mathbf{G}_g = \begin{bmatrix} 1 & 0 & 0 \end{bmatrix} \tag{41}$$

4.2. Algorithm modifications

During the pumping phase, the training procedure is only performed when, from an analytical point of view, current flows in the circuit ($i_p(t) > 0$). When there is no current, the system dynamics cannot be observed; therefore, the ASEKF stops and the state estimates are not updated. At the beginning of each correction step, when $i_{p,k}$ and u_k are measured, the following conditions are checked:

$$i_{p,k} < i_{th} = 50 \text{ mA} \tag{42}$$

$$u_k < 0 \text{ V} \tag{43}$$

If both conditions are verified, the correction is skipped: $\widehat{i}_{p,k|k}$ is constrained to zero and the other estimates are not corrected. The same conditions are introduced at the beginning of the prediction step, but with reference to the previous measurements, $i_{p,k-1}$ and u_{k-1}. If

they are met, the prediction is not performed: all state estimates are not updated. Condition (42) cannot be set equal to zero due to the measurement noise. Therefore, a threshold i_{th} is chosen according to the sensor specifications (Table 2).

4.3. Initialization of the ASEKFs

The initialization of the ASEKF algorithm is explained with reference to the pumping subsystem, but the same considerations apply to the other subsystems. To initialize the algorithm, it is necessary to define a first guess for the augmented state vector and its covariance matrix. This initial guess is considered as the first *a priori* augmented state estimate $\hat{z}_{1|0}^a$ having covariance matrix $P_{1|0}$. Therefore, the first prediction step is included in the initialization itself and during the first iteration $k = 1$ only the correction step is performed. The covariance $P_{1|0}$ is built as a diagonal matrix. Its diagonal contains the state estimates' variances, chosen according to the uncertainty on the states' initial guess. The variances are then large if there are many uncertainties about the guessed values or small if the initial values are fairly certain. The current i_p is observed and its guess can be set to a value close to the actual one, hence its variance is small. As for the augmented states, it is usually possible to make assumptions about the order of magnitude of the unknown parameters to be identified. Since the coffee machine is a household appliance, it includes small and lightweight electrical devices and motors. Accordingly, an initial value between 0.01 H and 1 H can be assumed for the electrical inductances. The electrical resistances can be initialized between 100 Ω and 1000 Ω, since the rms of the input voltage u is about 242.8 V and the current flowing in the circuits has a rms of less than 1 A (graphs (a) and (c) in Fig. 3). The variances for the unknown parameters are therefore set to high values because there is a lot of uncertainty about the initial states. It is preferable to have large variances for the augmented states, even a hundred or a thousand times the corresponding initial state, so that the algorithm can naturally converge to the values sought. The initial values of $P_{1|0}$ have little effect on the performance of the ASEKF, because this matrix is updated at each iteration; it fills up and stabilizes.

The process noise covariance matrix Q^a and the measurement noise covariance matrix R need to be defined. The implementation of the ASEKF can be challenging because of the difficulty in estimating these matrices. Since they are assumed to be constant, they strongly affect the filter behavior and must be tuned as accurately as possible. Particularly, the algorithm is very sensitive to even a small variation of R. Large values in R and small values in Q^a means that the model is more trustworthy than the measurements and vice versa; the right trade-off must be achieved.

The augmented covariance matrix Q^a is built as a diagonal matrix (uncorrelated noise processes). Each variance in the diagonal refers to a specific state. In equation (34), the current i_p evolves following the discretized dynamic model (26), while nothing is specified about the evolution of the unknown parameters (a discrete-time random-walk model is adopted). If model (26) is accurate, the variance $\sigma_{w_{i_p}}^2$ can be set small. The variances of the uncertain parameters must be large enough to introduce the right amount of probability and let the filter identify them. A first estimate can be obtained if the amplitude of variation of these parameters is known *a priori*. Since the resistance R_p is constant and the inductance L_p varies over time, $\sigma_{w_{L_p}}^2$ can be set larger than $\sigma_{w_{R_p}}^2$.

As there is only one observation, the current i_p, the matrix R degenerates into a scalar $\sigma_{v_{i_p}}^2$. The current measurement total uncertainty is estimated from the sensor specifications (Table 2) by combining the instrument accuracy (σ_a) and the measurement noise level (σ_n). The accuracy $\pm 3\%$ gives the peak-to-peak amplitude and corresponds to $\pm 3\sigma_a$. Since i_p varies from 0 A to about 1 A (Fig. 3), the reference reading is set at 1 A, so that in absolute terms the error is maximum. Therefore, the peak-to-peak amplitude is ± 30 mA and $\sigma_a = 10$ mA. The noise level 3 mV is given as a peak-to-peak amplitude on the output signal. Knowing the sensitivity, it is converted to 30 mA on the input signal, corresponding to $\sigma_n = 5$ mA. Sensor accuracy and measurement noise can be combined by adding up the individual errors (worst-case uncertainty) or by calculating the square root of the sum of the squares of the individual errors [73,74]. An estimate of $\sigma_{v_{i_p}}$ is obtained by picking a value between these sums: 15 mA and 11.2 mA.

The voltage u is not an observation exploited in the correction step of the ASEKF. Being measured, it is a noisy input. In a similar manner, the voltage measurement total uncertainty is estimated from the sensor specifications (Table 2), obtaining a worst-case uncertainty of about 2.14 V. The input u_{k-1} appears in state equation (34) and its uncertainty has a mitigated impact on the estimate $\hat{i}_{p,k|k-1}$ because u_{k-1} is multiplied by the ratio $\frac{\Delta t}{L_{p,k-1|k-1}} = 1.6 \times 10^{-3}$ s/H ($\Delta t = 1.6 \times 10^{-4}$ s and roughly $\hat{L}_{p,k-1|k-1} \cong 0.1$ H). This results in a standard deviation of 3.4 mA, which is considered within $\sigma_{w_{i_p}}$, since the process noise w^a is additive.

The initial guess for the augmented state vector and the covariance matrices chosen to initialize the ASEKF algorithm for each subsystem are listed in Table 4. Since L_u is constant and $\tilde{R}_u(t)$ varies over time, $\sigma_{w_{L_u}}^2$ can be set smaller than $\sigma_{w_{\tilde{R}_u}}^2$. Finding the appropriate $\hat{z}_{1|0}^a$, $P_{1|0}$, Q^a and R is an iterative procedure (trial and error) and an essential prerequisite for the algorithm convergence. Usually, a few

Table 4
Initialization of the ASEKFs.

Subsystem	Pumping	Grinding
$\hat{z}_{1|0}^a$	$\{1 \quad 1 \quad 200\}^T$	$\{1 \quad 1 \quad 200\}^T$
$P_{1|0}$	diag(1, 1000, 100000)	diag(10, 100, 1000)
Q^a	diag(1e-10, 1e-2, 1e-3)	diag(1e-10, 1e-8, 1e1)
R	0.015^2	0.015^2

calibration attempts are sufficient. Once convergence is achieved, state guess and covariances are fine-tuned to improve the identification process.

4.4. Identification results

The analyzed time windows of the three datasets for training the dynamic models are given in Table 5. The results are presented graphically for the first dataset.

A comparison between the observed current and that estimated by the algorithm during the pumping phase and grinding phase is illustrated in Figs. 5 and 6, respectively. The ASEKFs produce very accurate estimates, which track the observation, filtering out the measurement noise. In sections where the current estimate $\hat{i}_{p,k|k}$ is constrained to zero (Fig. 5), the sensor provides no useful information, only background noise (theoretically, there is no current in the circuit).

The type of measurement noise distribution can be assessed by calculating the difference between the measured current and the signal estimated by the ASEKF. The resulting errors can be represented in a histogram, to which is overlaid a plot of the probability density function of the normal distribution fitted to the error data. Figs. 7 and 8 show the estimation outcome for the measurement noise v_{i_p} (pumping phase) and v_{i_u} (grinding phase), respectively. Since both histograms quite closely follow the shape of the fitted probability density function, the noise sufficiently satisfies the filter's assumption of normal distribution with zero mean. In Fig. 7 the mean value of the fitted normal distribution is not exactly zero, but it is close to 0.01 A. This deviation is due to the fact that the estimate $\hat{i}_{p,k|k}$ tends to underestimate the measure in sections where $\hat{i}_{p,k|k}$ is constrained to zero (Fig. 5).

The identifications of R_p and L_p are shown in Figs. 9 and 10, respectively. As for the resistance R_p, complete convergence is not reached. However, a convergence value of about 250 Ω is expected, which is reasonable for this type of electrical device.

Graph (a) in Fig. 10 contains a zoom of the time trend identified for L_p, which is a periodic pattern at the same frequency as the voltage. Graph (b) in Fig. 10 displays the average trend of an inductance cycle, calculated by averaging over several cycles in the time window 35.6 s – 36.4 s, where convergence is already reached. At the beginning of each pumping cycle, the inductance L_p decreases: the piston is still going through the final part of the pumping stroke. As the current i_p rises, the electromagnetic force F_e also increases (equation (20)). When F_e overcomes the other forces acting on the piston, the latter reverses its motion and is pulled into the solenoid. As a result, L_p increases. The gray horizontal segments have no physical meaning (graph (a) in Fig. 10), as they correspond to the pumping cycle portion with zero current, where identification is not performed and the estimate is not updated. The identified L_p varies approximately between 0.6 H and 2.8 H. These values are slightly higher than those expected for this device (not exceeding 2 H) [55].

The identifications of L_u and $\widetilde{R}_u$ are illustrated in Figs. 11 and 12, respectively. A value of about 0.235 H is found for L_u. It is calculated as the curve average from 79.6 s to 81 s, where the estimate stabilizes around a certain constant value.

Graph (a) in Fig. 12 displays a zoom of the identified $\widetilde{R}_u$, which has a periodic time trend at the supply voltage frequency: the valleys alternate reaching two different minimum values. This pattern is governed by the motor speed ω_u and its periodicity is not affected by the chaotic load T_l. Graph (b) in Fig. 12 shows the average trend of a resistance cycle, computed by averaging over several periods in the time window 79.6 s – 81 s. The identified resistance $\widetilde{R}_u$ varies approximately between 290 Ω and 530 Ω. Alternatively, it is possible to consider a periodic trend with double the frequency, as the speed ω_u also depends on the electromagnetic torque T_e which pulsates at twice the voltage frequency (equation (33)).

To more thoroughly evaluate the chaotic load impact on motor dynamics, an auxiliary test (not necessary for training validation) was conducted by forcing the machine to perform grinding without coffee beans. The motor draws less power and the current rms decreases, because the cutters do not encounter resistance. However, the current signal exhibits an even more defined triangular waveform, meaning that there are also other phenomena causing non-linearity. The system could have variable inertia or the action of a speed limiter or controller could alter the motor dynamics [58], also affecting the armature current. It is convenient to improve the model accuracy by considering magnetic core saturation only if it is certain that the only component involved is a universal motor.

It must be emphasized that the equivalent circuits (Fig. 2) and the corresponding dynamic models are developed after making hypotheses about the nature of the subsystems' main components. These assumptions may not be entirely correct: the components are different or there are unknown secondary devices within the subsystems that are not accounted for in the models. The parameter values and patterns resulting from the identification may therefore deviate from those expected for the assumed electrical device and should be interpreted as equivalent parameters of the entire subsystem. Based on these considerations, all estimates are considered acceptable and tested for validation in Section 5.

4.4.1. Dataset comparison

The analyzed time windows of the three datasets to train the dynamic models and the resulting estimates of R_p and L_u are listed in

Table 5
Training results.

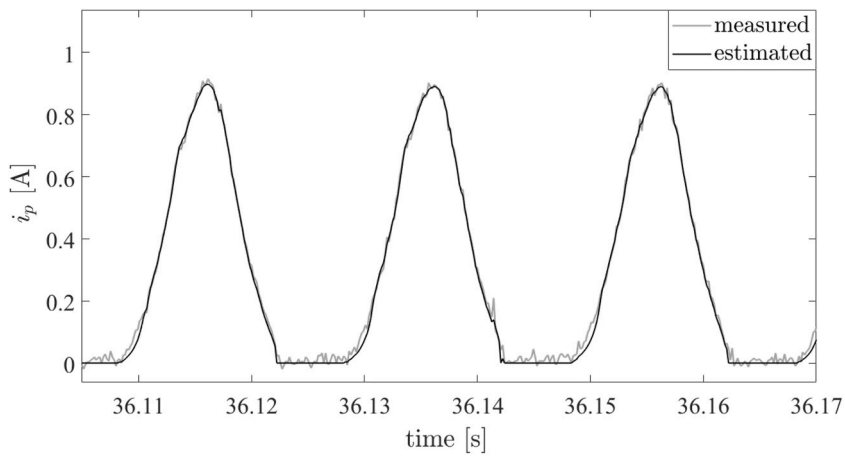| Dataset	coffee1	coffee2	coffee3
Pumping	34.8 s – 36.4 s	103.2 s – 104.4 s	26.6 s – 28.5 s
R_p [Ω]	250	252	251
Grinding	78.2 s – 81 s	6.3 s – 8 s	76.3 s – 77.8 s
L_u [H]	0.235	0.239	0.238

Fig. 5. Measured and estimated i_p comparison, 3-cycle zoom, pumping phase (*coffee1*).
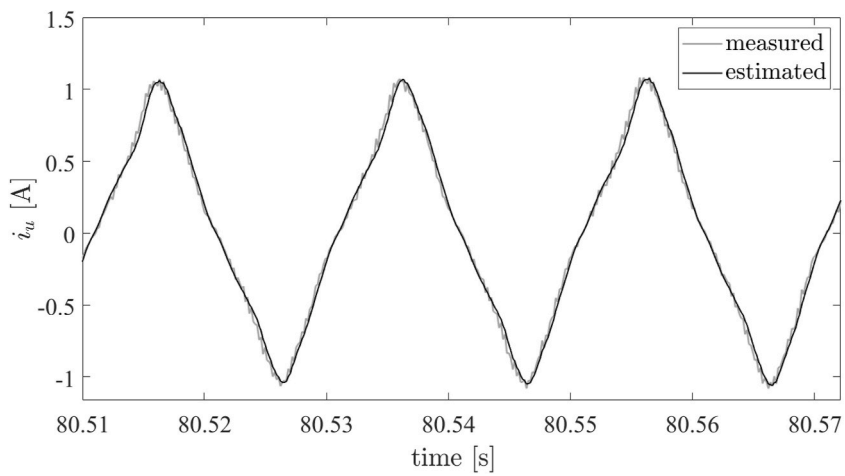

Fig. 6. Measured and estimated i_u comparison, 3-cycle zoom, grinding phase (*coffee1*).
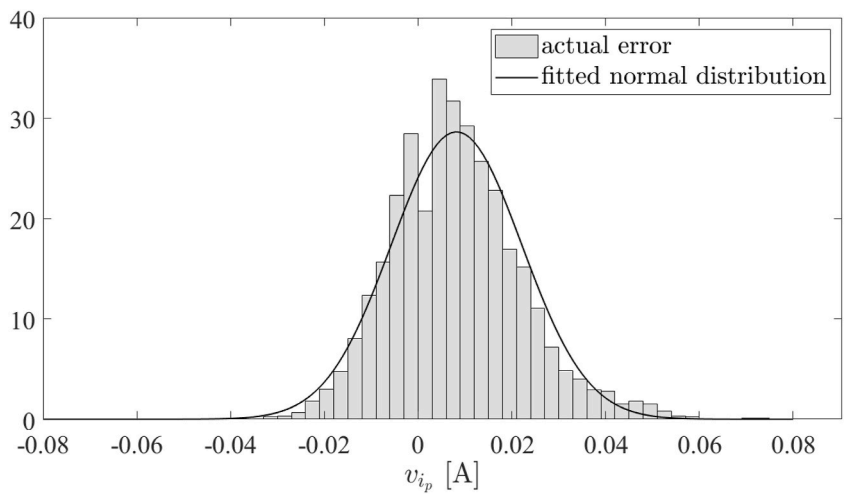

Fig. 7. Estimate of the measurement noise v_{i_p} distribution, pumping phase (*coffee1*).
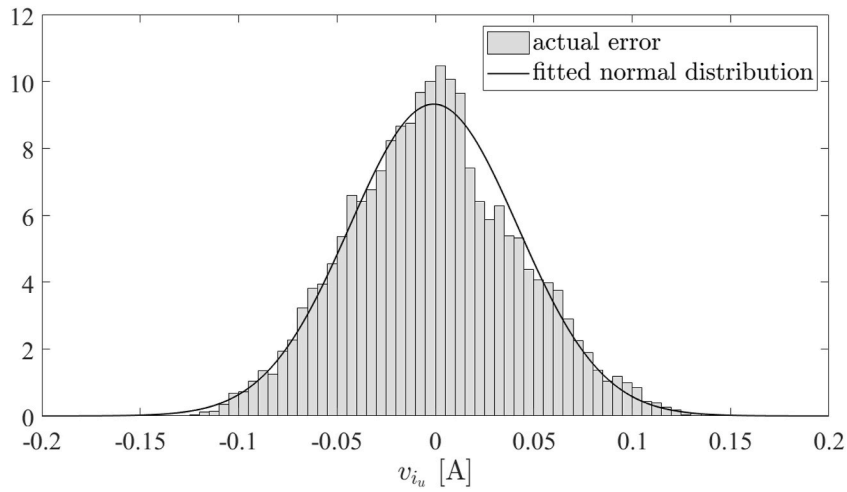
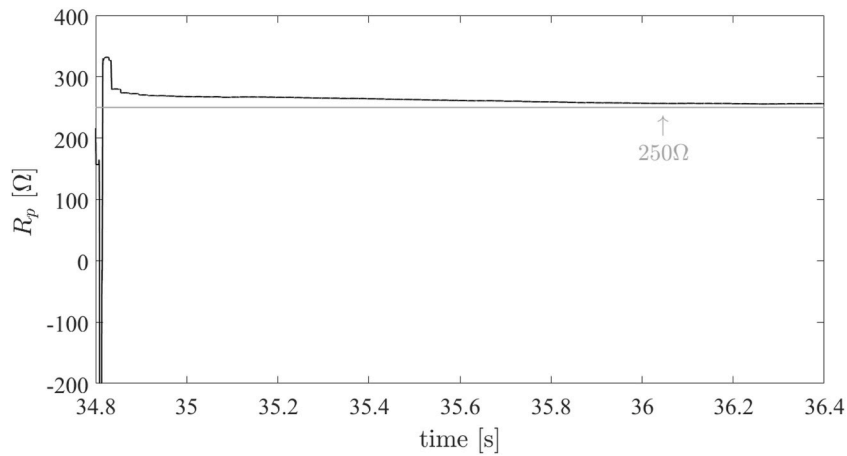**Fig. 8.** Estimate of the measurement noise v_{i_u} distribution, grinding phase (*coffee1*).

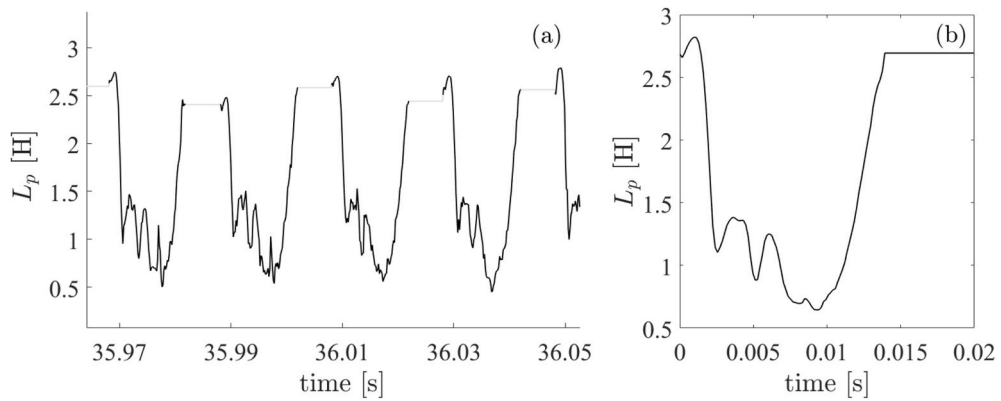**Fig. 9.** R_p identification (*coffee1*).

Fig. 10. L_p identification (*coffee1*): 4-cycle zoom (a), average trend (b).
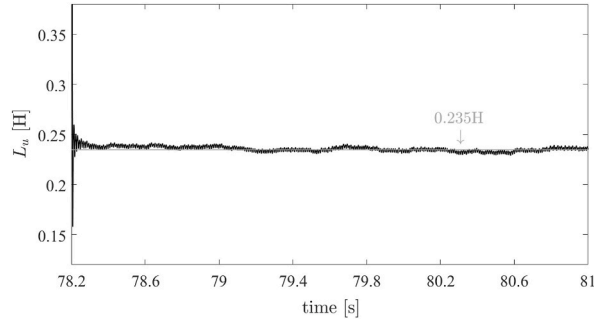
Fig. 11. L_u identification (*coffee1*).
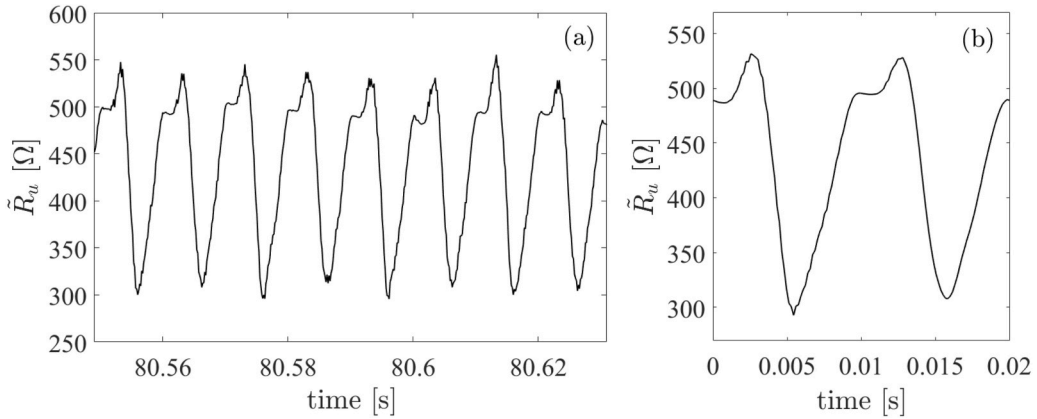
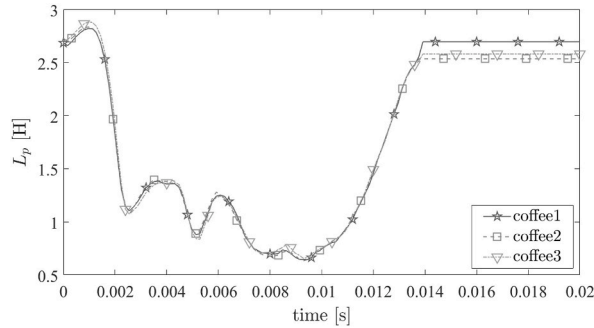**Fig. 12.** $\widetilde{R}_u$ identification (*coffee1*): 4-cycle zoom (a), average trend (b).

Fig. 13. L_p identification (all datasets).

Table 5. The time trends identified for L_p and $\widetilde{R}_u$ are compared with each other in Figs. 13 and 14, respectively. The training procedure provides similar outcomes for all analyzed datasets.

5. Power consumption prediction

The equivalent circuits trained in Section 4 need to be validated. Since the DT's purpose is to forecast the machine's electricity consumption, the validation test assesses the model's capability in reproducing the subsystem's actual energy use. The estimated power consumption is compared with the real one measured during the relevant elementary phase.

The actual instantaneous power p of the pumping and grinding subsystems is calculated from the voltage and current measurements of dataset *coffee1* (Fig. 2). The time windows analyzed comprise 20 voltage cycles and are listed in Table 6, together with the corresponding actual average power p_{ave}. These portions of the signals do not correspond to the pumping and grinding phases of *coffee1* examined to perform the first training: the time windows considered are different (Table 5).
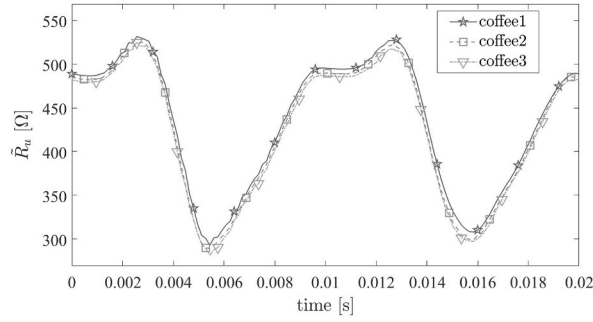
Fig. 14. $\widetilde{R}_u$ identification (all datasets).

Table 6
Actual power (*coffee1*).

Subsystem	Time window	p_{ave} [W]
Pumping	44.51 s – 44.91 s	53.23
Grinding	8.51 s – 8.91 s	152.92

By using the three sets of parameters identified from different acquisitions (Section 4.4.1), it is possible to provide three predictions of the appliance's instantaneous power during pumping and grinding. To make a reliable comparison, forecasts are performed through simulations under the same real supply conditions: the measured voltage u (from *coffee1* dataset) is used as input for the dynamic models. For each elementary phase, 20 cycles are simulated (about 0.4 s). The predicted instantaneous power $\widehat{p}$ is calculated by multiplying the measured voltage u by the current obtained via numerical integration of the dynamic model. Numerical integration is conducted by means of the MATLAB *ode45* solver, which is based on an explicit Runge-Kutta formula (4,5), the Dormand-Prince pair [75,76]. The simulation time step is equal to the time resolution of the data acquisition ($\Delta t = 1.6 \times 10^{-4}$ s). The prediction and validation test results are shown below.

The estimates of R_p and L_p are introduced into equation (22). The complete dynamic model (22-25) allows to simulate the pumping subsystem behavior and its power $\widehat{p}_p$. The three forecasts are compared with each other and with the measured power p_p in Fig. 15. The time axis is that of the simulation: the measurements are shifted along the time axis until they synchronize with the simulated curves. The largest gap between estimates and actual curve is found when the negative power approaches zero.

The estimates of $\widetilde{R}_u$ and L_u are fed into dynamic model (29), which is then used to simulate the grinding subsystem behavior and its power $\widehat{p}_u$. The comparison between the measured power p_u and the predicted ones is shown in Fig. 16. Slight deviations between actual and estimated values can be observed at peaks.

The prediction performance is assessed through the RMSE and CV- RMSE, calculated by means of equations (17) and (18), respectively. The resulting errors are listed in Table 7. The RMSE is scale-dependent and provides a direct quantification of the error, whereas the CV-RMSE is a scale-independent metric, useful for comparing performance between different systems and approaches. The RMSE in the pumping subsystem is lower than that in the grinding subsystem, because of the different power rating. In terms of CV-RMSE, the forecast performance for grinding is better than that for pumping, meaning that dynamic model (22) is more suitable than model (29) to represent the respective subsystem power consumption. However, both models are adequately close to physical reality for engineering purposes and achieve prediction accuracy levels that ML techniques can rarely guarantee [13]. Since the estimates correctly track the instantaneous powers, the equivalent circuits can be validated and chosen as representative of the electrical energy consumption of the corresponding phase.
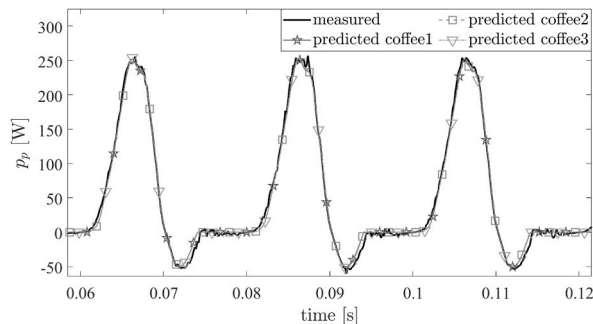

Fig. 15. Measured p_p and predicted $\widehat{p}_p$ comparison, pumping subsystem, 3-cycle zoom (all datasets).
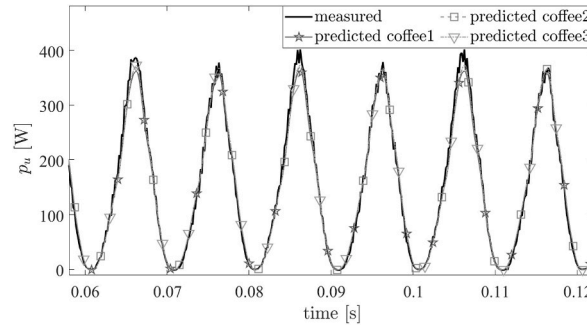
Fig. 16. Measured p_u and predicted $\hat{p}_u$ comparison, grinding subsystem, 3-cycle zoom (all datasets).

Table 7
Prediction performance.

Dataset	coffee1		coffee2		coffee3	
Subsystem	Pumping	Grinding	Pumping	Grinding	Pumping	Grinding
RMSE [W]	5.50	12.11	5.56	11.30	5.18	11.79
CV-RMSE	10.33%	7.92%	10.45%	7.39%	9.73%	7.71%
$\hat{p}_{ave}$ [W]	53.07	150.80	52.85	153.70	53.22	154.52
%err	0.30%	1.39%	0.71%	0.51%	0.02%	1.05%

Table 7 also shows the forecast of the average power consumed $\hat{p}_{ave}$ and the resulting percentage error (%err), which is not a reliable metric for a quantitative assessment: a low %err could be found even if the instantaneous power is improperly estimated.

A validated model can be used to simulate the subsystem's behavior under operating conditions and scenarios other than current ones, evaluating the impact on energy consumption due to variations of the control input or one or more parameters. This feature becomes even more attractive for multi-input systems. The variation in parameters may be related to degradation in component performance (due to wear or failures) or replacement of components by others with different characteristics. If the dynamic model has input-dependent parameters, a prediction performed with an input other than that of the training phase will be more approximate. The validation is conducted on a short-term scenario. However, the forecast horizon has no limits as long as a trend can be assumed or predicted for the system inputs.

6. Conclusions

In this paper, an effective tool based on DT for predicting electric power consumption of industrial production systems is proposed. The DT's innovative architecture integrates the ASEKF and non-intrusive sensors, enabling its practical implementation for partially known and difficult-to-access industrial manufacturing systems without special efforts. Such a structure ensures the identification of virtual model's unknown elements through short online training phases requiring small amounts of real-time raw data. This method offers significant potential in energy management and planning for optimizing consumption and improving energy efficiency in the manufacturing industry.

An experiment is conducted in offline mode on an automatic coffee machine and can serve as a blueprint to develop forecasting DTs for other industrial systems. The research results show a prediction accuracy not exceeding 10.5% in terms of CV-RMSE. DT's robustness and reliability are tested by feeding the ASEKF with different datasets, obtaining comparable outcomes for both model training and prediction performance.

The main direction of future research will concern the real-time synchronization between the DT and its original counterpart through ASEKFs, in order to test the technique also in online mode. Future work will also focus on integrating electromechanical coupling into the DT model and testing a multi-filter algorithm capable of dealing with complex phases, where several subsystems are operating simultaneously. By also introducing mechanical models, DTs can provide a comprehensive estimate of energy usage, tracking energy flow, evaluating system losses and efficiency, and forecasting the impact on electricity consumption due to load variations. Its application can therefore be extended to real-time monitoring for fault detection and predictive maintenance.

The proposed work exhibits some limitations:

- the availability of reliable measurements not affected by gross error, which are needed to discern whether a preliminary model is characterized by high or low bias and thus validate it for power consumption prediction;
- the ASEKF algorithm's assumption of Gaussian noise with zero mean, as in practice other types of noise distribution may be present;
- the expert knowledge required during model training for separating and labeling energy consumption sources and initializing the ASEKF.

The literature search for algorithms suitable to reduce human intervention at this stage and to be integrated into the DT will be the target of further studies.

Ethics declaration

Review and/or approval by an ethics committee was not needed for this study because it does not involve human and/or animal participants or material. Informed consent was not required for this study because it does not involve human participants or material.

Data availability

Data associated with this study have been deposited into a publicly available repository (open-source, accession number not required), hosted at Zenodo [45]: CAFFEINE Dataset, 2023, Zenodo, v1.1, URL: https://doi.org/10.5281/zenodo.8351431, by R. Delabeye, A. Baldassarre, C. B. Brahim, A. Kosecki, J.-L. Dion, M. Ghienne, O. Penas, F. Renaud, N. Peyret.

CRediT authorship contribution statement

A. Baldassarre: Writing – original draft, Visualization, Validation, Software, Methodology, Investigation, Formal analysis, Data curation. **J.-L. Dion:** Writing – review & editing, Supervision, Methodology, Funding acquisition, Conceptualization. **N. Peyret:** Writing – review & editing, Project administration, Methodology. **F. Renaud:** Software, Methodology, Formal analysis.

Declaration of competing interest

The authors declare the following financial interests/personal relationships which may be considered as potential competing interests: Antonio Baldassarre reports financial support was provided by European Commission (Horizon 2020 Industrial Leadership - Grant agreement 958478).

Acknowledgements

References

[1] International Energy Agency, Key World Energy Statistics 2020,, Paris,, Aug 2020,. URL iea.org/reports/key-world-energy-statistics-2020.
[2] International Energy Agency, World Energy Balances (2019), https://doi.org/10.1787/3a876031-en.
[3] Ritchie H., Roser M., Emissions by Sector, Our World in Data, 2020. ourworldindata.org/emissions-by-sector, (Accessed 11 September 2023).
[4] U.S. Energy Information Administration, International Energy Outlook (2021). eia.gov/outlooks/ieo/, 6-10-2021. URL.
[5] S. Debler, M. Berthou, R. Aubry, S. Palm, The factory of the future: two case studies to illustrate the role of energy in two industrial sectors, in: Proceedings of ECOS 2015 - The 28th International Conference, Jul 2015.
[6] X. Liu, O. Baiocchi, A comparison of the definitions for smart sensors, smart objects and Things in IoT, in: 2016 IEEE 7th Annual Information Technology, Electronics and Mobile Communication Conference (IEMCON), 2016, pp. 1–4, https://doi.org/10.1109/IEMCON.2016.7746311.
[7] J. Walther, M. Weigold, A systematic review on predicting and forecasting the electrical energy consumption in the manufacturing industry, Energies (2021).
[8] F. Tao, Q. Qi, A. Liu, A. Kusiak, Data-driven smart manufacturing, J. Manuf. Syst. 48 (2018) 157–169, https://doi.org/10.1016/j.jmsy.2018.01.006. Special Issue on Smart Manufacturing.
[9] H. Patel, M. Shah, Energy consumption and price forecasting through data-driven analysis methods: A review, SN Comput. Sci. 2 (4) (Jun 2021), https://doi.org/10.1007/s42979-021-00698-2.
[10] A. Bracale, G. Carpinelli, P. De Falco, T. Hong, Short-term industrial reactive power forecasting, Int. J. Electr. Power Energy Syst. 107 (2019) 177–185, https://doi.org/10.1016/j.ijepes.2018.11.022.
[11] D. Solyali, A comparative analysis of machine learning approaches for short-/long-term electricity load forecasting in Cyprus, Sustainability 12 (9) (2020), https://doi.org/10.3390/su12093612.
[12] M. Bahij, M. Labbadi, M. Cherkaoui, C. Chatri, A. Elkhatiri, A. Elouerghi, A review on the prediction of energy consumption in the industry sector based on machine learning approaches, in: 2021 4th International Symposium on Advanced Electrical and Communication Technologies (ISAECT), 2021, pp. 1–5, https://doi.org/10.1109/ISAECT53699.2021.9668559.
[13] Y. He, P. Wu, Y. Li, Y. Wang, F. Tao, Y. Wang, A generic energy prediction model of machine tools using deep learning algorithms, Appl. Energy 275 (2020) 115402, https://doi.org/10.1016/j.apenergy.2020.115402.
[14] C. Fan, F. Xiao, Y. Zhao, A short-term building cooling load prediction method using deep learning algorithms, Appl. Energy 195 (2017) 222–233, https://doi.org/10.1016/j.apenergy.2017.03.064.
[15] S. Bourhnane, M.R. Abid, R. Lghoul, K. Zine-dine, N. Elkamoun, D. Benhaddou, Machine learning for energy consumption prediction and scheduling in smart buildings, SN Appl. Sci. 2 (2020) 1–10.
[16] IBM, What is a Digital Twin? [accessed: 7-September-2023]. URL ibm.com/topics/what-is-a-digital-twin.
[17] C. Semeraro, M. Lezoche, H. Panetto, M. Dassisti, Digital twin paradigm: A systematic literature review, Comput. Ind. 130 (2021) 103469, https://doi.org/10.1016/j.compind.2021.103469.
[18] H. van der Valk, H. Haße, F. Möller, M. Arbter, J.-L. Henning, B. Otto, A taxonomy of digital twins, in: Americas Conference on Information Systems, 2020.
[19] F. Tao, J. Cheng, Q. Qi, M. Zhang, H. Zhang, F. Sui, Digital twin-driven product design, manufacturing and service with big data, Int. J. Adv. Des. Manuf. Technol. 94 (2018) 3563–3576.
[20] H. Sun, C. Li, X. Fang, H. Gu, Optimized throughput improvement of assembly flow line with digital twin online analytics, in: 2017 IEEE International Conference on Robotics and Biomimetics (ROBIO), 2017, pp. 1833–1837, https://doi.org/10.1109/ROBIO.2017.8324685.

[21] Q. Qiao, J. Wang, L. Ye, R.X. Gao, Digital Twin for machining tool condition prediction, in: Procedia CIRP, 52nd CIRP Conference on Manufacturing Systems (CMS), vol. 81, 2019, pp. 1388–1393, https://doi.org/10.1016/j.procir.2019.04.049. Ljubljana, Slovenia, June 12-14, 2019.

[22] Y. Huang, J. Tao, G. Sun, T. Wu, L. Yu, X. Zhao, A novel digital twin approach based on deep multimodal information fusion for aero-engine fault diagnosis, Energy 270 (2023) 126894, https://doi.org/10.1016/j.energy.2023.126894.

[23] C. Semeraro, H. Aljaghoub, M.A. Abdelkareem, A.H. Alami, M. Dassisti, A. Olabi, Guidelines for designing a digital twin for Li-ion battery: A reference methodology, Energy 284 (2023) 128699, https://doi.org/10.1016/j.energy.2023.128699.

[24] D. Zhong, Z. Xia, Y. Zhu, J. Duan, Overview of predictive maintenance based on digital twin technology, Heliyon 9 (4) (2023) e14534, https://doi.org/10.1016/j.heliyon.2023.e14534.

[25] W. Yu, P. Patros, B. Young, E. Klinac, T.G. Walmsley, Energy digital twin technology for industrial energy management: Classification challenges and future, Renew. Sustain. Energy Rev. 161 (2022) 112407, https://doi.org/10.1016/j.rser.2022.112407.

[26] C. Boje, A. Guerriero, S. Kubicki, Y. Rezgui, Towards a semantic construction digital twin: Directions for future research, Autom. ConStruct. 114 (2020) 103179, https://doi.org/10.1016/j.autcon.2020.103179.

[27] W. Kritzinger, M. Karner, G. Traar, J. Henjes, W. Sihn, Digital twin in manufacturing: A categorical literature review and classification, IFAC-PapersOnLine 51 (11) (2018) 1016–1022,, https://doi.org/10.1016/j.ifacol.2018.08.474, 16th IFAC Symposium on Information Control Problems in Manufacturing (INCOM), 2018.

[28] R. Delabeye, O. Penas, R. Plateaux, Scalable ontology-based V&V process for heterogeneous systems and applications, in: MODELS '22: Proceedings of the 25th International Conference on Model Driven Engineering Languages and Systems: Companion Proceedings, Montréal, Canada, 2022, https://doi.org/10.1145/3550356.3561577.

[29] R.E. Kalman, A new approach to linear filtering and prediction problems, Journal of Basic Engineering 82 (1) (1960) 35–45, https://doi.org/10.1115/1.3662552.

[30] C. Urrea, R. Agramonte, Kalman filter: historical overview and review of its use in robotics 60 years after its creation, J. Sens. 2021 (2021) 1016–1022, https://doi.org/10.1155/2021/9674015.

[31] F. Auger, M. Hilairet, J.M. Guerrero, E. Monmasson, T. Orlowska- Kowalska, S. Katsura, Industrial applications of the kalman filter: a review, IEEE Trans. Ind. Electron. 60 (12) (2013) 5458–5471, https://doi.org/10.1109/TIE.2012.2236994.

[32] W. Ma, P. Guo, X. Wang, Z. Zhang, S. Peng, B. Chen, Robust state of charge estimation for Li-ion batteries based on cubature Kalman filter with generalized maximum correntropy criterion, Energy 260 (2022) 125083, https://doi.org/10.1016/j.energy.2022.125083.

[33] Z. Liu, Z. Zhao, Y. Qiu, B. Jing, C. Yang, H. Wu, Enhanced state of charge estimation for Li-ion batteries through adaptive maximum correntropy Kalman filter with open circuit voltage correction, Energy 283 (2023) 128738, https://doi.org/10.1016/j.energy.2023.128738.

[34] J. Ren, Y. Xu, H. Zhang, F. Yang, Y. Yang, X. Wang, P. Jin, D. Huang, State of charge estimation of ultracapacitor based on forgetting factor recursive least square and extended Kalman filter algorithm at full temperature range, Heliyon 8 (11) (2022) e11146, https://doi.org/10.1016/j.heliyon.2022.e11146.

[35] R. Deaves, Covariance bounds for augmented state Kalman filter application, Electron. Lett. 35 (2) (1999) 2062–2064.

[36] E. Lourens, E. Reynders, G. De Roeck, G. Degrande, G. Lombaert, An augmented Kalman filter for force identification in structural dynamics, Mech. Syst. Signal Process. 27 (2012) 446–460, https://doi.org/10.1016/j.ymssp.2011.09.025.

[37] J.-L. Dion, C. Stephan, G. Chevallier, H. Festjens, Tracking and removing modulated sinusoidal components: a solution based on the kurtosis and the extended Kalman filter, Mech. Syst. Signal Process. 38 (2) (2013) 428–439, https://doi.org/10.1016/j.ymssp.2013.04.001.

[38] D. Simon, Optimal State Estimation: Kalman, H Infinity, and Nonlinear Approaches, Wiley, 2006.

[39] S. Vettori, E. Di Lorenzo, B. Peeters, M. Luczak, E. Chatzi, An adaptive-noise augmented Kalman filter approach for input-state estimation in structural dynamics, Mech. Syst. Signal Process. 184 (2023) 109654, https://doi.org/10.1016/j.ymssp.2022.109654.

[40] T.P. Bohlin, Practical Grey-Box Process Identification: Theory and Applications, Advances in Industrial Control, Springer London, 2006.

[41] B. Sohlberg, E.W. Jacobsen, Grey box modelling – branches and experiences, IFAC Proc. 41 (2) (2008) 11415–11420,, https://doi.org/10.3182/20080706-5-KR-1001.01934, 17th IFAC World Congress.

[42] ETAM29.62X - Bean to Cup Espresso and Cappuccino Machine - Instruction for Use, De'Longhi Appliances. URL delonghi.com/it-it/manuals/macchina-da-caffe-automatic a-autentica-plus-etam29-620-sb/p/ETAM29.620.SB.

[43] S.N. Vukosavic, Electrical Machines, Power Electronics and Power Systems, Springer, New York, 2012.

[44] L. Meirovitch, Fundamentals of Vibrations, McGraw-Hill higher education, McGraw-Hill, 2001.

[45] Delabeye R., Baldassarre A., Brahim C.B., Kosecki A., Dion J.-L., Ghienne M., Penas O., Renaud F., Peyret N., Zenodo, CAFFEINE Dataset, v1.1 (2023), doi: 10.5281/zenodo.8351431. URL https://doi.org/10.5281/zenodo.8351431.

[46] M. Petracco, Percolation, in: A. Illy, R. Viani (Eds.), Espresso Coffee: the Science of Quality, Elsevier Science, 2005, pp. 259–289. Ch. 7.

[47] Qualité de l'Électricité , Commission de Régulation de l'Énergie (CRE) (23-06-2023) (Accessed 17 August 2023).

[48] Clark C., Vibration Pump vs Rotary Pump in Espresso Machines, Brew Coffee at Home, 21-06-2022. brewcoffeehome.com/vibration-pump-vs-rotary-pump/ (Accessed 10 August 2023).

[49] V.A. Neelakantan, P.G. Otanez, S. Bai, Low Noise High Efficiency Solenoid Pump, US20120251359A1, GM Global Technology Operations LLC, 2012. patents.google.com/patent/US20120251359A1/en.

[50] R. Rayner, Pump Users Handbook, Elsevier Science, 1995.

[51] S.E. Lyshevski, Electromechanical Systems and Devices, Taylor & Francis, 2008.

[52] A.M. Hosseini, S. Arzanpour, F. Golnaraghi, A.M. Parameswaran, Solenoid actuator design and modeling with application in engine vibration isolators, J. Vib. Control 19 (7) (2013) 1015–1023, https://doi.org/10.1177/1077546311435517.

[53] Understanding Solenoid Design & Function, Tameson [accessed: 10-August- 2023]. URL tameson.com/pages/solenoid.

[54] P. Schimpf, A detailed explanation of solenoid force, Int. J. Recent Trends Eng. Technol. 8 (2013) 7–14.

[55] I. Riaz, Vibration reduction of solenoid pump by feedback control system [Master's Thesis], Politecnico di Milano, 2019. hdl.handle.net/10589/149372.

[56] K.E. Atkinson, An Introduction to Numerical Analysis, Wiley, 1978.

[57] M. Petracco, Grinding, in: A. Illy, R. Viani (Eds.), Espresso Coffee: the Science of Quality, Elsevier Science, 2005, pp. 215–229. Ch. 5.

[58] Coffee Machine Motor Technology and Complete Solutions, Shenzhen Power Motor Industrial Co. [accessed: 12-August-2023]. URL power-motor.com/HomeAppliances/CoffeeMachineMotorSol ution.html.

[59] T.S. Bindschedler, Universal Motor, US1860728A, Unisys Corp, 1925. patents.google.com/patent/US1860728A/en.

[60] H. Grop, Modelling of a universal motor with speed control [Master's Thesis], Royal Institute of Technology, Stockholm, 2006.

[61] Universal Motor (Complete Guide), Electrical4u online [accessed: 13- August-2023]. URL electrical4uonline.com/universal-motor/.

[62] S.L. Herman, Delmar's Standard Textbook of Electricity, Cengage Learning, 2010.

[63] S. Moreau, J.-C. Trigeassou, Modelling and identification of a non-linear saturated magnetic circuit: theoretical study and experimental results, Math. Comput. Simulat. 71 (4) (2006) 446–459,, https://doi.org/10.1016/j.matcom.2006.02.006. Modeling and Simulation of Electric Machines, Converters and Systems.

[64] Understanding magnetic saturation and its effects, Electrical4U, 2023. electrical4u.com/magnetic-saturation/ (Accessed 12 August 2023).

[65] P.S. Bimbhra, Electrical Machinery, Khanna Publishers, 2003.

[66] A.S. Zein El Din, M.E. El-Shebiny, M.M. Khater, Microcomputer-controlled universal motor, in: Proceedings of IEEE International Symposium on Industrial Electronics, vol. 2, 1996, pp. 653–658, https://doi.org/10.1109/ISIE.1996.551019, 2.

[67] B. Bonnländer, R. Eggers, U.H. Engelhardt, H.G. Maier, Roasting, in: A. Illy, R. Viani (Eds.), Espresso Coffee: the Science of Quality, Elsevier Science, 2005, pp. 179–214. Ch. 4.

[68] L.G. Austin, O. Trass, Size reduction of solids crushing and grinding equipment, in: M. Fayed, L. Otten (Eds.), Handbook of Powder Science & Technology, Springer US, 1997, pp. 586–634. Ch. 12.

[69] T. Tanaka, Y. Kanda, Powder handling and operations: crushing and grinding, in: H. Masuda, K. Higashitani, H. Yoshida (Eds.), Powder Technology Handbook, CRC Press, 2006, pp. 503–526. Ch. 5.1.

[70] D.W. Hart, Power Electronics, McGraw-Hill, 2010.

[71] Full wave rectifier: what is it? (Formula and circuit diagram), Electrical4U, 2021. electrical4u.com/full-wave-rectifiers/ (Accessed 12 August 2023).

[72] Heater Resistor, EEPower, EETech Media [accessed: 19-August-2023]. URL eepower.com/resistor-guide/resistor-applications/heater-resistor/#.

[73] Voltage measurement accuracy, self-calibration, and ratiometric measurements [white Paper], Campbell Scientific, 2001.

[74] B.N. Taylor, C.E. Kuyatt, Guidelines for evaluating and expressing the uncertainty of NIST measurement results, NIST Technical Note 1297 (1994).

[75] J. Dormand, P. Prince, A family of embedded Runge-Kutta formulae, J. Comput. Appl. Math. 6 (1) (1980) 19–26, https://doi.org/10.1016/0771-050X(80)90013-3.

[76] L.F. Shampine, M.W. Reichelt, The MATLAB ODE suite, SIAM J. Sci. Comput. 18 (1) (1997) 1–22, https://doi.org/10.1137/S1064827594276424.